

# Local–global mode interaction in stringer-stiffened plates\*

M. Ahmer Wadee and Maryam Farsi

Department of Civil & Environmental Engineering,  
Imperial College London,  
London SW7 2AZ, UK

## Abstract

A recently developed nonlinear analytical model for axially loaded thin-walled stringer-stiffened plates based on variational principles is extended to include local buckling of the main plate. Interaction between the weakly stable global buckling mode and the strongly stable local buckling mode is highlighted. Highly unstable post-buckling behaviour and a progressively changing wavelength in the local buckling mode profile is observed under increasing compressive deformation. The analytical model is compared against both physical experiments from the literature and finite element analysis conducted in the commercial code ABAQUS; excellent agreement is found both in terms of the mechanical response and the predicted deflections.

## Key words

Mode interaction; Stiffened plates; Cellular buckling; Snaking; Nonlinear mechanics.

## 1 Introduction

Thin-walled stringer-stiffened plates under axial compression are well known to be vulnerable to buckling where local and global modes interact nonlinearly (Koiter & Pignataro, 1976; Fok *et al.*, 1976; Budiansky, 1976; Thompson & Hunt, 1984). However, since stiffened plates are highly mass-efficient structural components, their application is ubiquitous in long-span bridge decks (Ronalds, 1989), ships and offshore structures (Murray, 1973), and aerospace structures (Butler *et al.*, 2000; Loughlan, 2004). Hence, understanding the behaviour of these components represents a structural problem of enormous practical significance (Grondin *et al.*, 1999; Sheikh *et al.*, 2002; Ghavami & Khedmati, 2006). Other

---

\*Article accepted for *Thin-Walled Structures*, 19 September 2014.

significant structural components such as sandwich struts (Hunt & Wadee, 1998), built-up columns (Thompson & Hunt, 1973), corrugated plates (Pignataro *et al.*, 2000) and other thin-walled components (Hancock, 1981; Schafer, 2002; Becque & Rasmussen, 2009; Wadee & Bai, 2014) are also well-known to suffer from the instabilities arising from the interaction of global and local buckling modes.

In the authors' recent work (Wadee & Farsi, 2014), the aforementioned problem was studied using an analytical approach by considering that interactive buckling was wholly confined to the stringer (or stiffener) only. So-called “cellular buckling” (Hunt *et al.*, 2000; Wadee & Gardner, 2012; Wadee & Bai, 2014; Bai & Wadee, 2014) or “snaking” (Woods & Champneys, 1999; Burke & Knobloch, 2007; Chapman & Kozyreff, 2009) was captured, where snap-backs in the response, showing sequential destabilization and restabilization and a progressive spreading of the initial localized buckling mode, were revealed. The results showed reasonably good comparisons with a finite element (FE) model formulated in the commercial code ABAQUS (2011). The current work extends the previous model such that the interaction between global Euler buckling and the local buckling of the main plate, as well as the stiffener, are accounted. A system of nonlinear ordinary differential equations subject to integral constraints is derived using variational principles and is subsequently solved using the numerical continuation package AUTO-07P (Doedel & Oldeman, 2011). The relative rigidity of the main plate–stiffener joint is adjusted by means of a rotational spring, increasing the stiffness of which results in the erosion of the snap-backs that signify cellular buckling. However, the changing local buckling wavelength is still observed, although the effect is not quite so marked as compared with the case where the joint is assumed to be pinned (Wadee & Farsi, 2014). A finite element model is also developed using the commercial code ABAQUS for validation purposes. Moreover, given that local buckling of the main plate is included alongside the buckling of the stiffener in the current model, which is often observed in experiments, the present results are also compared with a couple of physical test results from the literature (Fok *et al.*, 1976). The comparisons turn out to be excellent both in terms of the mechanical response and the physical post-buckling profiles.

## 2 Analytical Model

Consider a thin-walled simply-supported plated panel that has uniformly spaced stiffeners above and below the main plate, as shown in Figure 1, with panel length  $L$  and the spacing between the stiffeners being  $b$ . It is made from a linear elastic, homogeneous and isotropic material with Young's modulus  $E$ , Poisson's ratio  $\nu$  and shear modulus  $G = E/[2(1 + \nu)]$ . If the panel is much wider than long, *i.e.*  $L \ll n_s b$ , where  $n_s$  is the number of stiffeners in the panel, the critical buckling behaviour of the panel would be strut-like with a half-sine wave eigenmode along the length. Moreover, this would allow a portion of the panel that is representative of its entirety to be isolated as a strut as depicted in Figure 1, since the transverse bending curvature of the panel during initial post-buckling would be relatively small.

Therefore, the current article presents an analytical model of a representative portion

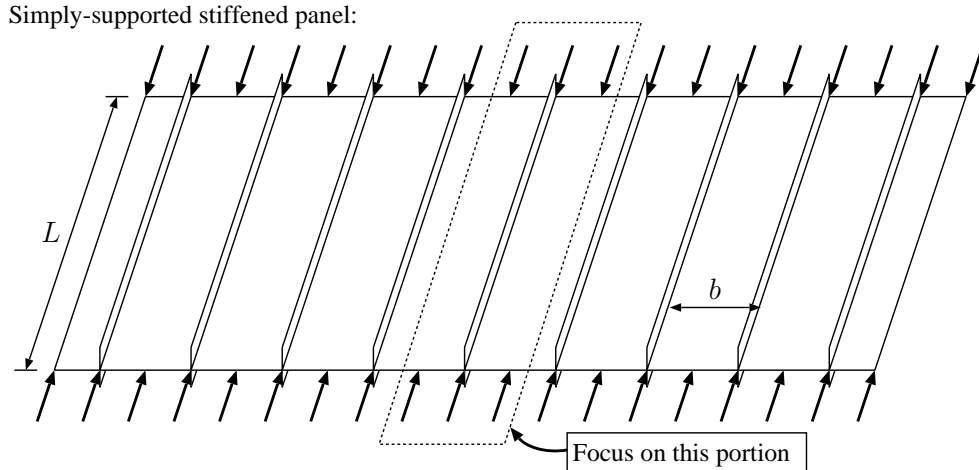


Figure 1: An axially compressed simply-supported stiffened panel of length  $L$  and evenly spaced stiffeners separated by a distance  $b$ .

of an axially-compressed stiffened panel, which simplifies to a simply supported strut with geometric properties defined in Figure 2. The strut has length  $L$  and comprises a main plate (or skin) of width  $b$  and thickness  $t_p$  with two attached longitudinal stiffeners of heights  $h_1$  and  $h_2$  with thickness  $t_s$ , as shown in Figure 2(b). The axial load  $P$  is applied at the centroid of the whole cross-section denoted as the distance  $\bar{y}$  from the centre line of the plate. The rigidity of the connection between the main plate and stiffeners is modelled with a rotational spring of stiffness  $c_p$ , as shown in Figure 2(c). If  $c_p = 0$ , a pinned joint is modelled, but if  $c_p$  is large, the joint is considered to be completely fixed or rigid. Note that the rotational spring with stiffness  $c_p$  only stores strain energy by local bending of the stiffener or the main plate at the joint coordinates  $(x = 0, y = -\bar{y})$  and not by rigid body rotation of the entire joint in a twisting action.

## 2.1 Modal descriptions

To model interactive buckling analytically, it has been demonstrated that shear strains need to be included (Wadee & Hunt, 1998; Wadee *et al.*, 2010) and for thin-walled metallic elements Timoshenko beam theory has been shown to be sufficiently accurate (Wadee & Gardner, 2012; Wadee & Bai, 2014). To model the global buckling mode, two degrees of freedom, known as “sway” and “tilt” in the literature (Hunt *et al.*, 1988), are used. The sway mode is represented by the displacement  $W$  of the plane sections that are under global flexure and the tilt mode is represented by the corresponding angle of inclination  $\theta$  of the plane sections, as shown in Figure 2(d). From linear theory, it can be shown that  $W(z)$  and  $\theta(z)$  may be represented by the following expressions (Hunt *et al.*, 1988):

$$W(z) = -q_s L \sin \frac{\pi z}{L}, \quad \theta(z) = q_t \pi \cos \frac{\pi z}{L}, \quad (1)$$

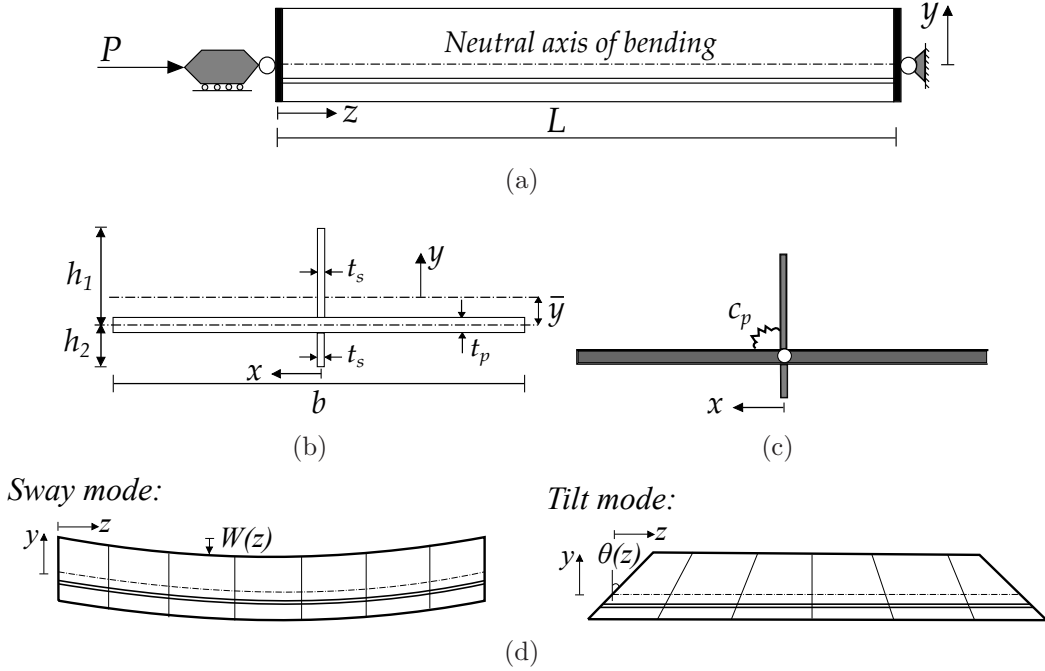


Figure 2: (a) Elevation of the representative portion of the stiffened plate modelled as strut of length  $L$  that is compressed axially by a force  $P$ . (b) Strut cross-section geometry. (c) Modelling the joint rigidity of the main plate–stiffener connection with a rotational spring of stiffness  $c_p$ . (d) Sway and tilt components of the global buckling mode.

where the quantities  $q_s$  and  $q_t$  are the generalized coordinates of the sway and tilt components respectively. The corresponding shear strain  $\gamma_{yz}$  during bending is given by the following expression:

$$\gamma_{yz} = \frac{dW}{dz} + \theta = -(q_s - q_t) \pi \cos \frac{\pi z}{L}. \quad (2)$$

In the current model, only geometries are chosen where global buckling about the  $x$ -axis is critical.

The kinematics of the local buckling modes for the stiffener and the plate are modelled with appropriate boundary conditions. A linear distribution in  $y$  for the local in-plane displacement  $u(y, z)$  is assumed due to Timoshenko beam theory:

$$u(y, z) = Y(y)u(z), \quad (3)$$

where  $Y(y) = (y + \bar{y})/h_1$ , as depicted in Figure 3(a).

Formulating the assumed deflected shape, however, for out-of-plane displacements of the stiffener  $w(y, z)$  and the main plate  $w_p(x, z)$ , see Figure 3(b), the stiffness of the rotational spring  $c_p$ , depicted in Figure 2(c), is considered. The role of the spring is to resist the rotational distortion from the relative bending of the main plate and the stiffener with respect to the original rigid body configuration. The shape of the local buckling mode along the depth of the stiffener and along the width of the main plate can be therefore

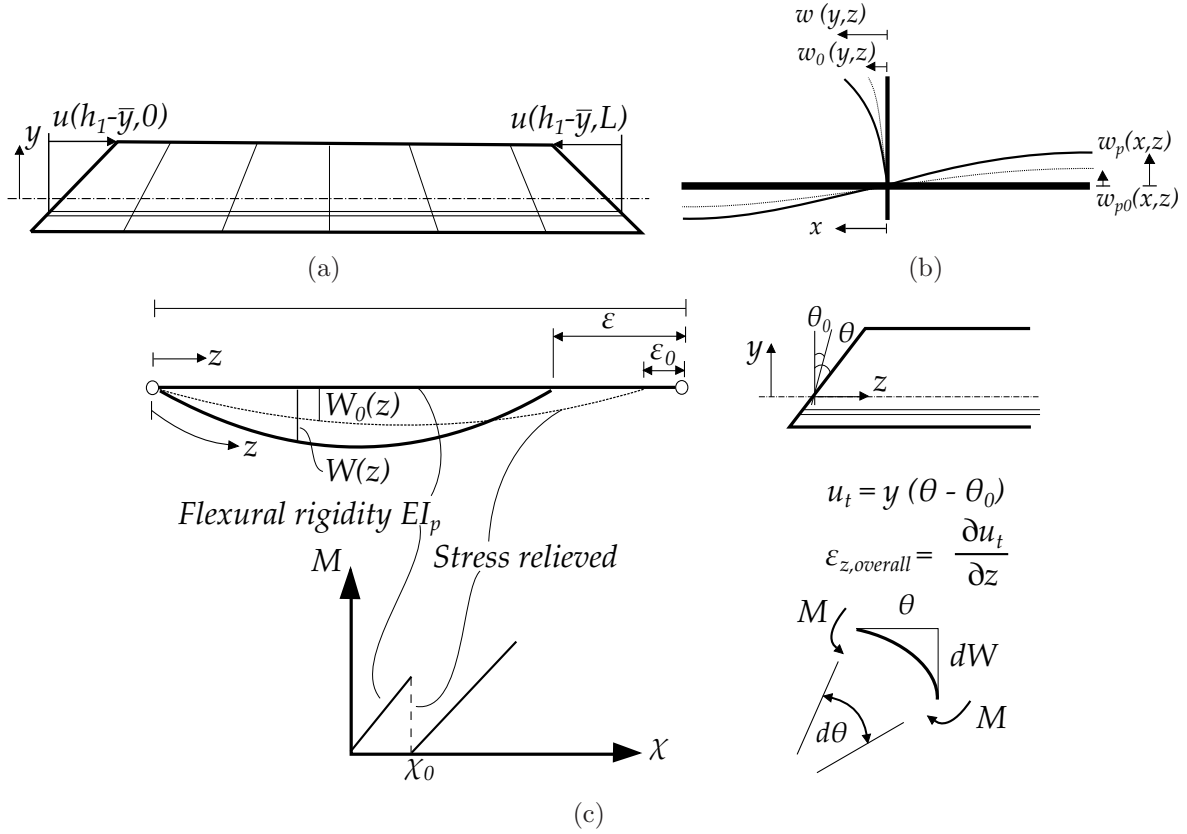


Figure 3: (a) Local in-plane deflection of the stiffener  $u(y, z)$ . (b) Local out-of-plane deflection of the stiffener  $w_s(y, z)$  with the initial imperfection  $w_0(y, z)$  and local out-of-plane deflection of the plate  $w_p(x, z)$  with the initial imperfection  $w_{p0}(x, z)$ . (c) Introduction of the global imperfection functions  $W_0$  and  $\theta_0$ ; for the local imperfections,  $w_0$  or  $w_{p0}$  would replace  $W_0$  and apply only to the stiffener or the main plate respectively.

estimated, using the Rayleigh–Ritz method (Guarracino & Walker, 1999), by a nonlinear function that is a summation of both polynomial and trigonometric terms. The general form of these approximations can be expressed by the following relationships:

$$w(y, z) = f(y)w(z), \quad w_p(x, z) = g(x)w_p(z), \quad (4)$$

where:

$$\begin{aligned} f(y) &= B_0 + B_1 Y + B_2 Y^2 + B_3 Y^3 + B_4 \sin(\pi Y), \\ g(x) &= C_0 + C_1 X + (-1)^i C_2 X^2 + C_3 X^3 + C_4 \sin(\pi X), \end{aligned} \quad (5)$$

and  $X(x) = x/b$ . Moreover, for  $i = 1$ , the range  $x = [0, b/2]$  and for  $i = 2$ , the range  $x = [-b/2, 0]$ . For  $f(y)$ , the constant coefficients  $B_0, B_1, B_2, B_3$  and  $B_4$  are determined by applying appropriate boundary conditions for the stiffener. At the junction between the stiffener and the main plate,  $y = -\bar{y}$ , the conditions are:

$$w(y, z) = 0, \quad -D_s \frac{\partial^2}{\partial y^2} w(y, z) = c_p \frac{\partial}{\partial y} w(y, z) \quad (6)$$

if the main plate does not rotate, whereas at the stiffener tip,  $y = h_1 - \bar{y}$ , the conditions are:

$$D_s \frac{\partial^2}{\partial y^2} w(y, z) = 0, \quad D_s \frac{\partial^3}{\partial y^3} w(y, z) = 0. \quad (7)$$

For  $g(x)$ , the constant coefficients  $C_0, C_1, C_2, C_3$  and  $C_4$  are determined by applying appropriate boundary conditions for the main plate. At the junction between the stiffener and the main plate,  $x = 0$ , the conditions are:

$$w_p(x, z) = 0, \quad -D_p \frac{\partial^2}{\partial x^2} w_p(x, z) = c_p \frac{\partial}{\partial x} w_p(x, z) \quad (8)$$

if the stiffener does not rotate, whereas at the tips of the main plate at  $x = b/2$  and  $x = -b/2$ , the conditions of which are subtly different from those given in Equation (7) and are thus:

$$\frac{\partial}{\partial x} w_p(x, z) = 0, \quad D_p \frac{\partial^3}{\partial x^3} w_p(x, z) = 0, \quad (9)$$

where  $D_s$  and  $D_p$  are the stiffener and the plate flexural rigidities given by the expressions  $Et_s^3/[12(1-\nu^2)]$  and  $Et_p^3/[12(1-\nu^2)]$  respectively. It is worth emphasizing that the second (mechanical) boundary conditions for determining  $B_n$  and  $C_n$ , given in Equations (6) and (8), are simplifying approximations that are admissible since the formulation is based essentially on the Rayleigh–Ritz method (Guarracino & Walker, 1999).

The length  $\bar{y}$  gives the location of the neutral-axis of bending measured from the centre line of the main plate and is expressed thus:

$$\bar{y} = \frac{t_s [h_1^2 - h_2^2]}{2 [(b - t_s) t_p + (h_1 + h_2) t_s]}. \quad (10)$$

The final constants are fixed by imposing the normalizing conditions with  $f(h_1 - \bar{y}) = 1$  and  $g(b/2) = 1$ . The functions for the deflected shapes  $w(y, z)$  and  $w_p(x, z)$  can be written thus:

$$\begin{aligned} w(y, z) &= \left\{ Y - J_s \frac{\pi^3}{6} \left[ 2Y - 3Y^2 + Y^3 - \frac{6}{\pi^3} \sin(\pi Y) \right] \right\} w(z), \\ w_p(x, z) &= - \left\{ \sin(\pi X) + J_p \left[ X + (-1)^i X^2 - \frac{1}{4} \sin(\pi X) \right] \right\} w_p(z), \end{aligned} \quad (11)$$

where:

$$J_s = \left\{ \pi \left[ \frac{D_s \pi^2}{c_p h_1} + \frac{\pi^2}{3} - 1 \right] \right\}^{-1}, \quad J_p = \left\{ \left[ \frac{1}{4} - \frac{2D_p}{c_p b \pi} - \frac{1}{\pi} \right] \right\}^{-1}. \quad (12)$$

In physical experiments, it is often observed that the main plate deflects in sympathy with the stiffener to some extent and so in the current work, the following relationship is assumed,  $w_p(z) = \lambda_p w(z)$ . Since the rotations would therefore be all in the same sense they can be expressed as first derivatives of  $w$  or  $w_p$ ; these are multiplied by the joint rotational stiffness  $c_p$  such that the total bending moment is established. By allowing both the main plate and the stiffener to rotate locally and summing the bending moments for

the stiffener and both sides of the main plate at the intersection ( $x = 0, y = -\bar{y}$ ), an explicit relationship can be derived:

$$D_s \frac{\partial^2 w}{\partial y^2} + D_p \frac{\partial^2 w_p}{\partial x^2} \Big|_{i=1} - D_p \frac{\partial^2 w_p}{\partial x^2} \Big|_{i=2} = c_p \left( \frac{\partial w}{\partial y} + \frac{\partial w_p}{\partial x} \Big|_{i=1} + \frac{\partial w_p}{\partial x} \Big|_{i=2} \right). \quad (13)$$

The negative sign in front of the final term of the left hand side of Equation (13) reflects the fact the main plate bending moment changes sign at  $x = 0$ . The expression for the deflection relating parameter  $\lambda_p$  can be determined by substituting the aforementioned expression  $w_p(z) = \lambda_p w(z)$  into Equation (13) and, after a bit of manipulation, the following relationship is derived:

$$\lambda_p = \left( \frac{2b^2}{3h_1^2} \right) \left[ \frac{c_p h_1 [3 + J_s \pi (3 - \pi^2)] - 3D_s J_s \pi^3}{8D_p J_p + c_p b [4\pi + J_p (4 - \pi)]} \right]. \quad (14)$$

This simplifies the formulation considerably by allowing the system to be modelled with effectively only one out-of-plane displacement function  $w$ .

## 2.2 Imperfection modelling

Since real structures contain imperfections, the current model incorporates the possibility of both global and local initial imperfections within the geometry. This is performed by introducing initial deflections that are stress-relieved, as shown in Figure 3(c), such that the strain energies are zero in the initially imperfect state. An initial out-of-straightness  $W_0$  is introduced as a global imperfection as well as the corresponding initial rotation of the plane section  $\theta_0$  of the stiffener. The expressions for these functions are:

$$W_0(z) = -q_{s0} L \sin \frac{\pi z}{L}, \quad \theta_0 = q_{t0} \pi \cos \frac{\pi z}{L}, \quad (15)$$

with  $q_{s0}$  and  $q_{t0}$  defining the amplitudes of the global imperfection. The local out-of-plane imperfection for the stiffener and the main plate is formulated from a first order approximation of a multiple scale perturbation analysis of a strut on a softening elastic foundation (Wadee *et al.*, 1997), the mathematical shape of which is expressed as:

$$w_0(z) = A_0 \operatorname{sech} \left[ \frac{\alpha (z - \eta)}{L} \right] \cos \left[ \frac{\beta \pi (z - \eta)}{L} \right], \quad (16)$$

where  $z = [0, L]$  and  $w_0$  is symmetric about  $z = \eta$ . This function has been shown in the literature to provide a representative imperfection for local–global mode interaction problems (Wadee, 2000). Moreover, this form for  $w_0$  enables the study of periodic and localized imperfections; a local imperfection is periodic when  $\alpha = 0$  with a number of half sine waves equal to  $\beta$  along the length of the panel. It is also noted that the relationship between  $w_{p0}$  and  $w_0$  corresponds to that for the perfect case; hence,  $w_{p0} = \lambda_p w_0$  is assumed. The shape of the initial imperfection is illustrated in Figure 4. By increasing the  $\alpha$  value, the initial imperfection forms into a localized shape, as shown in Figure 4(a), otherwise the imperfection shape is periodic, as shown in Figure 4(b).

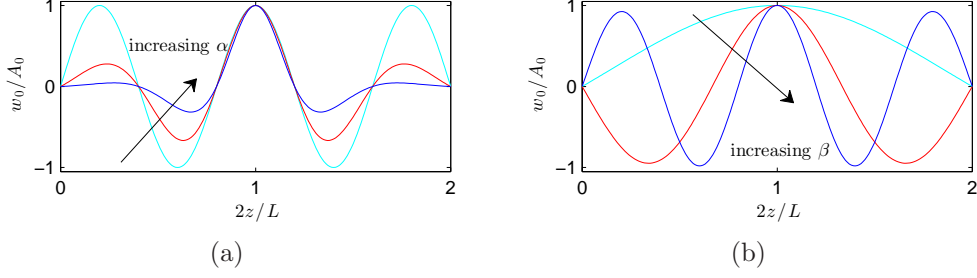


Figure 4: Local imperfection profile  $w_0$ . (a) Localized imperfections introduced by increasing  $\alpha$ . (b) Periodic imperfections ( $\alpha = 0$ ) with different numbers of half sine waves by changing  $\beta$ . In both cases  $\eta = L/2$ .

### 2.3 Total potential energy

A well established procedure for deriving the total potential energy  $V$ , has been presented in previous work (Wadee & Farsi, 2014); the current work follows the same approach but now includes the local buckling deflection of the main plate. The global strain energy  $U_{bo}$  due to Euler buckling is given by the equation below:

$$U_{bo} = \frac{1}{2}EI_p \int_0^L (\ddot{W} - \ddot{W}_0)^2 dz = \frac{1}{2}EI_p \int_0^L (q_s - q_{s0})^2 \frac{\pi^4}{L^2} \sin^2 \frac{\pi z}{L} dz, \quad (17)$$

where dots represent differentiation with respect to  $z$  and  $I_p = (b - t_s)t_p^3/12 + (b - t_s)t_p\bar{y}^2$  is the second moment of area of the plate about the global  $x$ -axis. The strain energy from local bending of the stiffener and the main plate  $U_{bl}$  is given by the following expression:

$$\begin{aligned} U_{bl} &= \frac{D_s}{2} \int_0^L \int_{-\bar{y}}^{h_1 - \bar{y}} \left\{ \left[ \frac{\partial^2(w - w_0)}{\partial z^2} + \frac{\partial^2(w - w_0)}{\partial y^2} \right]^2 \right. \\ &\quad \left. - 2(1 - \nu) \left[ \frac{\partial^2(w - w_0)}{\partial z^2} \frac{\partial^2(w - w_0)}{\partial y^2} - \left( \frac{\partial^2(w - w_0)}{\partial z \partial y} \right)^2 \right] \right\} dy dz \\ &\quad + \frac{D_p}{2} \int_0^L \int_{-b/2}^{b/2} \left\{ \left[ \frac{\partial^2(w_p - w_{p0})}{\partial z^2} + \frac{\partial^2(w_p - w_{p0})}{\partial x^2} \right]^2 \right. \\ &\quad \left. - 2(1 - \nu) \left[ \frac{\partial^2(w_p - w_{p0})}{\partial z^2} \frac{\partial^2(w_p - w_{p0})}{\partial x^2} - \left( \frac{\partial^2(w_p - w_{p0})}{\partial z \partial x} \right)^2 \right] \right\} dx dz, \\ &= \frac{D_s}{2} \int_0^L \left[ \{f^2\}_y (\ddot{w} - \ddot{w}_0)^2 + \{f''^2\}_y (w - w_0)^2 + 2\nu \{f f''\}_y (w - w_0)(\ddot{w} - \ddot{w}_0) \right. \\ &\quad \left. + 2(1 - \nu) \{f'^2\}_y (\dot{w} - \dot{w}_0)^2 \right] dz + \frac{D_p}{2} \int_0^L \left[ \{g^2\}_x (\ddot{w}_p - \ddot{w}_{p0})^2 + \{g''^2\}_x (w_p - w_{p0})^2 \right. \\ &\quad \left. + 2\nu \{g g''\}_x (w_p - w_{p0})(\ddot{w}_p - \ddot{w}_{p0}) + 2(1 - \nu) \{g'^2\}_x (\dot{w}_p - \dot{w}_{p0})^2 \right] dz. \end{aligned} \quad (18)$$

The terms within the braces are definite integrals, thus:

$$\{F(y)\}_y = \int_{-\bar{y}}^{h_1-\bar{y}} F(y) dy, \quad \{H(x)\}_x = \int_{-b/2}^{b/2} H(x) dx, \quad (19)$$

where  $F$  and  $H$  are example functions representing the actual expressions within the braces and primes denote differentiation with respect to the subscript outside the closing brace.

The membrane energy  $U_m$  is derived from the direct strains ( $\varepsilon$ ) and shear strains ( $\gamma$ ) in the plate and the stiffener. It is thus:

$$\begin{aligned} U_m &= U_d + U_s \\ &= \frac{1}{2} \int_0^L \left\{ \int_{-t_s/2}^{t_s/2} \left[ \int_{-\bar{y}}^{h_1-\bar{y}} (E\varepsilon_{zt}^2 + G\gamma_{yzt}^2) dy + \int_{-(h_2+\bar{y})}^{-\bar{y}} (E\varepsilon_{zb}^2 + G\gamma_{yzb}^2) dy \right] dx \right. \\ &\quad \left. + \int_{-t_p/2}^{t_p/2} \int_{-(b-t_s)/2}^{(b-t_s)/2} E\varepsilon_{zp}^2 dx dy \right\} dz. \end{aligned} \quad (20)$$

Note that the transverse component of the strain  $\varepsilon_y$  is neglected since it has been shown that it has no effect on the post-buckling behaviour of a long plate with three simply-supported edges and one free edge (Koiter & Pignataro, 1976). The global buckling contribution for the longitudinal strain  $\varepsilon_z$  can be obtained from the tilt component of the global mode, which is given by:

$$\varepsilon_{z,\text{global}} = y \frac{\partial \theta}{\partial z} = -y (q_t - q_{t0}) \frac{\pi^2}{L} \sin \frac{\pi z}{L}. \quad (21)$$

The local mode contribution is based on von Kármán plate theory (Bulson, 1970). A pure in-plane compressive strain  $\Delta$  is also included. The combined expressions for the direct strains for the top and bottom stiffeners  $\varepsilon_{zt}$  and  $\varepsilon_{zb}$  respectively, and for the main plate  $\varepsilon_{zp}$  are given thus:

$$\begin{aligned} \varepsilon_{zt} &= -y (q_t - q_{t0}) \frac{\pi^2}{L} \sin \frac{\pi z}{L} - \Delta + \frac{\partial u}{\partial z} + \frac{1}{2} \left( \frac{\partial w}{\partial z} \right)^2 - \frac{1}{2} \left( \frac{\partial w_0}{\partial z} \right)^2, \\ &= -y (q_t - q_{t0}) \frac{\pi^2}{L} \sin \frac{\pi z}{L} - \Delta + Y \dot{u} + \frac{1}{2} \{f^2\}_y (\dot{w}^2 - \dot{w}_0^2), \\ \varepsilon_{zb} &= -y (q_t - q_{t0}) \frac{\pi^2}{L} \sin \frac{\pi z}{L} - \Delta \\ \varepsilon_{zp} &= -\Delta + \frac{1}{2} \left( \frac{\partial w_p}{\partial z} \right)^2 - \frac{1}{2} \left( \frac{\partial w_{p0}}{\partial z} \right)^2. \end{aligned} \quad (22)$$

The membrane energy contribution from the direct strains  $U_d$  is therefore:

$$\begin{aligned}
U_d = \frac{1}{2}Et_s \int_0^L \left\{ \frac{1}{3} [(h_1 - \bar{y})^3 + (h_2 + \bar{y})^3] (q_t - q_{t0})^2 \frac{\pi^4}{L^2} \sin^2 \frac{\pi z}{L} + \Delta^2 (h_1 + h_2) \right. \\
+ [(h_1 - \bar{y})^2 - (h_2 + \bar{y})^2] \Delta (q_t - q_{t0}) \frac{\pi^2}{L} \sin \frac{\pi z}{L} \\
+ h_1 \left[ \frac{1}{3} \dot{u}^2 + \frac{1}{4h_1} \{f^4\}_y (\dot{w}^2 - \dot{w}_0^2)^2 + \left\{ \frac{Yf^2}{h_1} \right\}_y \dot{u} (\dot{w}^2 - \dot{w}_0^2) \right] \\
- (q_t - q_{t0}) \frac{h_1 \pi^2}{L} \sin \frac{\pi z}{L} \left[ \left( \frac{2}{3} h_1 - \bar{y} \right) \dot{u} + \frac{1}{h_1} \{yf^2\}_y (\dot{w}^2 - \dot{w}_0^2) \right] \\
- h_1 \Delta \left[ \dot{u} + \frac{1}{h_1} \{f^2\}_y (\dot{w}^2 - \dot{w}_0^2) \right] \\
\left. + \left( \frac{t_p}{t_s} \right) \left[ (b - t_s) \Delta^2 + \frac{1}{4} \{g^4\}_x (\dot{w}_p^2 - \dot{w}_{p0}^2)^2 - \Delta \{g^2\}_x (\dot{w}_p^2 - \dot{w}_{p0}^2) \right] \right\} dz. \tag{23}
\end{aligned}$$

The membrane energy contribution from shear strains arises from those in the main plate  $\gamma_{xz}$  as well those in the stiffeners  $\gamma_{yz}$ ; the respective general expressions being:

$$\begin{aligned}
\gamma_{xz} &= \frac{\partial w_p}{\partial z} \frac{\partial w_p}{\partial x} - \frac{\partial w_{p0}}{\partial z} \frac{\partial w_{p0}}{\partial x}, \\
\gamma_{yz} &= \frac{\partial}{\partial z} (W - W_0) + (\theta - \theta_0) + \frac{\partial u}{\partial y} + \frac{\partial w}{\partial z} \frac{\partial w}{\partial y} - \frac{\partial w_0}{\partial z} \frac{\partial w_0}{\partial y}, \tag{24}
\end{aligned}$$

hence, the expressions for the top and bottom stiffeners and the plate are given respectively:

$$\begin{aligned}
\gamma_{yzt} &= - [(q_s - q_{s0}) - (q_t - q_{t0})] \pi \cos \frac{\pi z}{L} + \frac{u}{h_1} + \{ff'\}_y (w\dot{w} - w_0\dot{w}_0), \\
\gamma_{yzb} &= - [(q_s - q_{s0}) - (q_t - q_{t0})] \pi \cos \frac{\pi z}{L}, \tag{25}
\end{aligned}$$

with the explicit expression for the main plate shear strain:

$$\gamma_{xz} = \{gg'\}_x (w_p \dot{w}_p - w_{p0} \dot{w}_{p0}). \tag{26}$$

The membrane energy contribution from the shear strains  $U_s$  is therefore:

$$\begin{aligned}
U_s = \frac{1}{2}Gt_s \int_0^L \left\{ [(q_s - q_{s0}) - (q_t - q_{t0})]^2 \pi^2 \cos^2 \frac{\pi z}{L} (h_1 + h_2) \right. \\
+ \frac{1}{h_1} \left[ u^2 + h_1 \{(ff')^2\}_y (w\dot{w} - w_0\dot{w}_0)^2 + 2\{ff'\}_y u (w\dot{w} - w_0\dot{w}_0) \right] \\
- [(q_s - q_{s0}) - (q_t - q_{t0})] \left[ 2u + 2\{ff'\}_y (w\dot{w} - w_0\dot{w}_0) \right] \pi \cos \frac{\pi z}{L} \\
\left. + \left( \frac{t_p}{t_s} \right) \{ (gg')^2 \}_x (w_p \dot{w}_p - w_{p0} \dot{w}_{p0})^2 \right\} dz. \tag{27}
\end{aligned}$$

The final component of strain energy is that stored in the rotational spring of stiffness  $c_p$  representing the rigidity of the main plate–stiffener joint. It is given thus:

$$\begin{aligned} U_{sp} &= \frac{1}{2}c_p \int_0^L \left\{ \left[ \frac{\partial}{\partial y} [w(-\bar{y}, z) - w_0(-\bar{y}, z)] - \frac{\partial}{\partial x} [w_p(0, z) - w_{p0}(0, z)] \right]^2 \right\} dz, \\ &= \frac{1}{2}c_p \int_0^L \left\{ \left[ f'(-\bar{y})(w - w_0) - g'(0)(w_p - w_{p0}) \right]^2 \right\} dz, \end{aligned} \quad (28)$$

where  $f'(-\bar{y})$  and  $g'(0)$  indicate the values of  $f'$  and  $g'$  at  $y = -\bar{y}$  (or  $Y = 0$ ) and  $x = 0$  respectively. The final component of  $V$  is the work done by the axial load  $P$ , which is given by:

$$P\mathcal{E} = \frac{P}{2} \int_0^L \left[ 2\Delta + q_s^2 \pi^2 \cos^2 \frac{\pi z}{L} - 2 \left( \frac{h_2 + \bar{y}}{h_1 + h_2} \right) \dot{u} \right] dz, \quad (29)$$

where the end-displacement  $\mathcal{E}$  comprises components from pure squash, sway from global buckling and the component from local buckling of the stiffener. Therefore, the total potential energy  $V$  is given by the summation of all the strain energy terms minus the work done, thus:

$$V = U_{bo} + U_{bl} + U_m + U_{sp} - P\mathcal{E}. \quad (30)$$

## 2.4 Variational Formulation

The governing equations of equilibrium are obtained by performing the calculus of variations on the total potential energy  $V$  following the well established procedure presented in previous work (Hunt & Wadee, 1998; Wadee & Farsi, 2014). The integrand of the total potential energy  $V$  can be expressed as the Lagrangian ( $\mathcal{L}$ ) of the form:

$$V = \int_0^L \mathcal{L}(\ddot{w}, \dot{w}, w, \dot{u}, u, z) dz, \quad (31)$$

of course, this is after substituting the relationship,  $w_p = \lambda_p w$ . Hence, the first variation of  $V$  is:

$$\delta V = \int_0^L \left[ \frac{\partial \mathcal{L}}{\partial \ddot{w}} \delta \ddot{w} + \frac{\partial \mathcal{L}}{\partial \dot{w}} \delta \dot{w} + \frac{\partial \mathcal{L}}{\partial w} \delta w + \frac{\partial \mathcal{L}}{\partial \dot{u}} \delta \dot{u} + \frac{\partial \mathcal{L}}{\partial u} \delta u \right] dz. \quad (32)$$

To determine the equilibrium states,  $V$  must be stationary, hence the first variation  $\delta V$  must vanish for any small change in  $w$  and  $u$ . Since  $\delta \ddot{w} = d(\delta \dot{w})/dz$ ,  $\delta \dot{w} = d(\delta w)/dz$  and similarly  $\delta \dot{u} = d(\delta u)/dz$ , integration by parts allows the development of the Euler–Lagrange equations for  $w$  and  $u$ ; these comprise a fourth-order and a second-order non-linear differential equation for  $w$  and  $u$  respectively. To facilitate the solution within the package AUTO-07P, the variables are rescaled with respect to the non-dimensional spatial coordinate  $\tilde{z}$ , defined as  $\tilde{z} = 2z/L$ . Similarly, non-dimensional out-of-plane and in-plane displacements  $\tilde{w}$  and  $\tilde{u}$  are defined with the scalings  $2w/L$  and  $2u/L$  respectively. Note that the scalings exploit symmetry about midspan and the equations are hence solved for half the strut length; this assumption has been shown to be perfectly acceptable for cases

where global buckling is critical (Wadee, 2000). The non-dimensional differential equations for  $w$  and  $u$  are thus:

$$\begin{aligned}
& \left[ 1 + \lambda_p^2 \left( \frac{t_p}{t_s} \right)^3 \frac{\{g^2\}_x}{\{f^2\}_y} \right] \left( \ddot{w} - \ddot{w}_0 \right) + \frac{L^2}{2\{f^2\}_y} \left\{ \left[ \nu \{ff''\}_y - (1 - \nu) \{f'^2\}_y \right] \right. \\
& \quad \left. + \lambda_p^2 \left( \frac{t_p}{t_s} \right)^3 \left[ \nu \{gg''\}_x - (1 - \nu) \{g'^2\}_x \right] \right\} (\tilde{w} - \tilde{w}_0) + \tilde{k} (\tilde{w} - \tilde{w}_0) \\
& - \tilde{D} \left[ \frac{\{f^4\}_y}{\{f^2\}_y} (3\tilde{w}^2\tilde{w} - \tilde{w}\tilde{w}_0^2 - 2\tilde{w}_0\tilde{w}_0\tilde{w}) + \frac{\{2Yf^2\}_y}{\{f^2\}_y} (\tilde{u}\tilde{w} + \tilde{w}\tilde{u}) \right. \\
& \quad \left. - 2\Delta\tilde{w} - 2(q_t - q_{t0}) \frac{\pi^2}{L} \frac{\{yf^2\}_y}{\{f^2\}_y} \left( \sin \frac{\pi\tilde{z}}{2} \tilde{w} + \frac{\pi}{2} \cos \frac{\pi\tilde{z}}{2} \tilde{w} \right) \right] \\
& - \frac{\tilde{G}L^2\tilde{w}}{2\{f^2\}_y} \left[ \{(ff')^2\}_y (\tilde{w}^2 + \tilde{w}\tilde{w} - \tilde{w}_0^2 - \tilde{w}_0\tilde{w}_0) + \frac{1}{h_1} \{ff'\}_y \tilde{u} \right. \\
& \quad \left. + [(q_s - q_{s0}) - (q_t - q_{t0})] \frac{\pi^2}{L} \{ff'\}_y \sin \frac{\pi\tilde{z}}{2} \right] \\
& - \left( \frac{t_p}{t_s} \right) \frac{\tilde{D}\lambda_p^2}{\{f^2\}_y} \left[ \lambda_p^2 \{g^4\}_x (3\tilde{w}^2\tilde{w} - \tilde{w}\tilde{w}_0^2 - 2\tilde{w}_0\tilde{w}_0\tilde{w}) - 2\Delta\{g^2\}_x \tilde{w} \right] \\
& - \left( \frac{t_p}{t_s} \right) \frac{L^2\tilde{G}\lambda_p^4\tilde{w}}{2\{f^2\}_y} \left[ \{(gg')^2\}_x (\tilde{w}^2 + \tilde{w}\tilde{w} - \tilde{w}_0^2 - \tilde{w}_0\tilde{w}_0) \right] = 0, \tag{33}
\end{aligned}$$

$$\begin{aligned}
& \tilde{u} - \frac{3\tilde{G}}{4\tilde{D}}\psi \left[ \psi (\tilde{u} + \{ff'\}_y (\tilde{w}\tilde{w} - \tilde{w}_0\tilde{w}_0)) - 2\pi [(q_s - q_{s0}) - (q_t - q_{t0})] \cos \frac{\pi\tilde{z}}{2} \right] \\
& - \left\{ \frac{3Yf^2}{h_1} \right\}_y (\tilde{w}\tilde{w} + \tilde{w}_0\tilde{w}_0) + \frac{1}{2} (q_t - q_{t0}) \pi^3 \left( \psi - \frac{3\bar{y}}{2L} \right) \cos \frac{\pi\tilde{z}}{2} = 0, \tag{34}
\end{aligned}$$

where the non-dimensional parameters are defined thus:

$$\begin{aligned}
\tilde{D} &= \frac{Et_s L^2}{8D_s}, \quad \tilde{G} = \frac{Gt_s L^2}{8D_s}, \\
\tilde{k} &= \frac{L^4}{16\{f^2\}_y} \left[ \{f''^2\}_y + \lambda_p^2 (t_p/t_s)^3 \{g''^2\}_x + c_p [f'(-\bar{y}) - \lambda_p g'(0)]^2 / D_s \right], \tag{35}
\end{aligned}$$

and  $\tilde{w}_0 = 2w_0/L$ ,  $\psi = L/h_1$ . There are further equilibrium conditions that relate to  $V$  being minimized with respect to the generalized coordinates  $q_s$ ,  $q_t$  and  $\Delta$ . This leads to the derivation of three integral conditions in non-dimensional form as follows:

$$\begin{aligned}
\frac{\partial V}{\partial q_s} &= \pi^2 (q_s - q_{s0}) + \tilde{s} [(q_s - q_{s0}) - (q_t - q_{t0})] - \frac{PL^2}{EI_p} q_s \\
& - \frac{\tilde{s}\tilde{\phi}}{2\pi} \int_0^2 \cos \frac{\pi\tilde{z}}{2} \left[ \tilde{u} + \{ff'\}_y (\tilde{w}\tilde{w} - \tilde{w}_0\tilde{w}_0) \right] d\tilde{z} = 0, \tag{36}
\end{aligned}$$

$$\begin{aligned} \frac{\partial V}{\partial q_t} = & \pi^2 (q_t - q_{t0}) + \tilde{\Gamma}_3 \Delta - \tilde{t} [(q_s - q_{s0}) - (q_t - q_{t0})] - \frac{1}{2} \int_0^2 \left\{ \sin \frac{\pi \tilde{z}}{2} \left[ \tilde{\Gamma}_1 \tilde{u} \right. \right. \\ & \left. \left. + \tilde{\Gamma}_2 (\tilde{w}^2 - \tilde{w}_0^2) \right] + \frac{\tilde{t} \tilde{\phi}}{\pi} \cos \frac{\pi \tilde{z}}{L} \left[ \tilde{u} + \{f f'\}_y (\tilde{w} \tilde{w} - \tilde{w}_0 \tilde{w}_0) \right] \right\} d\tilde{z} = 0, \end{aligned} \quad (37)$$

$$\begin{aligned} \frac{\partial V}{\partial \Delta} = & \Delta \left[ 1 + \frac{h_2}{h_1} + \frac{t_p(b - t_s)}{t_s h_1} \right] - \frac{P}{E t_s h_1} + (q_t - q_{t0}) \frac{\pi}{L h_1} [(h_1 - \bar{y})^2 - (h_2 + \bar{y})^2] \\ & - \frac{1}{4} \int_0^2 \left[ \tilde{u} + \frac{1}{h_1} \{f^2\}_y (\tilde{w}^2 - \tilde{w}_0^2) \right] d\tilde{z} - \left( \frac{t_p}{t_s} \right) \frac{\lambda_p^2}{4 h_1} \int_0^2 \left[ \{g^2\}_x (\tilde{w}^2 - \tilde{w}_0^2) \right] d\tilde{z} = 0. \end{aligned} \quad (38)$$

where the rescaled quantities are defined thus:

$$\begin{aligned} \tilde{\Gamma}_1 = & \frac{L h_1 (2h_1 - 3\bar{y})}{(h_1 - \bar{y})^3 + (h_2 + \bar{y})^3}, & \tilde{\Gamma}_2 = & \frac{3L \{y f^2\}_y}{(h_1 - \bar{y})^3 + (h_2 + \bar{y})^3}, \\ \tilde{\Gamma}_3 = & \frac{6L [(h_1 - \bar{y})^2 - (h_2 + \bar{y})^2]}{\pi [(h_1 - \bar{y})^3 + (h_2 + \bar{y})^3]}, & \tilde{\phi} = & \frac{L}{h_1 + h_2}, \\ \tilde{s} = & \frac{G t_s (h_1 + h_2) L^2}{E I_p}, & \tilde{t} = & \frac{3GL^2 (h_1 + h_2)}{E [(h_1 - \bar{y})^3 + (h_2 + \bar{y})^3]}. \end{aligned} \quad (39)$$

Since the stiffened panel is an integral member, Equation (38) provides a relationship linking  $q_s$  and  $q_t$  before any interactive buckling occurs, *i.e.* when  $w = u = 0$ . This relationship is also assumed to hold between  $q_{s0}$  and  $q_{t0}$ , which has the beneficial effect of reducing the number of imperfection amplitude parameters to one; this relationship is given by:

$$q_{s0} = (1 + \pi^2/\tilde{t}) q_{t0}. \quad (40)$$

The boundary conditions for  $\tilde{w}$  and  $\tilde{u}$  and their derivatives are for pinned conditions for  $\tilde{z} = 0$  and for reflective symmetry at  $\tilde{z} = 1$ :

$$\tilde{w}(0) = \tilde{w}'(0) = \tilde{w}(1) = \tilde{w}'(1) = \tilde{u}(1) = 0, \quad (41)$$

with a further condition from matching the in-plane strain:

$$\frac{1}{3} \tilde{u}(0) + \frac{1}{2} \left\{ \frac{Y}{h_1} f^2 \right\}_y [\tilde{w}^2(0) - \tilde{w}_0^2(0)] - \frac{1}{2} \Delta + \frac{P}{E t_s h_1} \left( \frac{h_2 + \bar{y}}{h_1 + h_2} \right) = 0. \quad (42)$$

Linear eigenvalue analysis for the perfect column ( $q_{s0} = q_{t0} = 0$ ) is conducted to determine the critical load for global buckling  $P_o^C$ . This is achieved by considering the Hessian matrix  $\mathbf{V}_{ij}$ , thus:

$$\mathbf{V}_{ij} = \begin{bmatrix} \frac{\partial^2 V}{\partial q_s^2} & \frac{\partial^2 V}{\partial q_s \partial q_t} \\ \frac{\partial^2 V}{\partial q_t \partial q_s} & \frac{\partial^2 V}{\partial q_t^2} \end{bmatrix}, \quad (43)$$

where the matrix  $\mathbf{V}_{ij}$  is singular at the global critical load  $P_o^C$ . Hence, the critical load for global buckling is:

$$P_o^C = \frac{\pi^2 EI_p}{L^2} \left[ 1 + \frac{\tilde{s}}{\pi^2 + \tilde{t}} \right]. \quad (44)$$

If the limit  $G \rightarrow \infty$  is taken, which represents a principal assumption in Euler–Bernoulli bending theory, it can be shown that the critical load expression converges to the Euler buckling load for the modelled strut, as would be expected.

### 3 Numerical results

Numerical results with a varying rotational spring stiffness  $c_p$  are now presented for the perfect system. The continuation and bifurcation software AUTO-07P (Doedel & Oldeman, 2011) is used to solve the complete system of equilibrium equations presented in the previous section. An example set of section and material properties are chosen thus:  $L = 5000$  mm,  $b = 120$  mm,  $t_p = 2.4$  mm,  $t_s = 1.2$  mm,  $h_1 = 38$  mm,  $h_2 = 1.2$  mm,  $E = 210$  kN/mm<sup>2</sup>,  $\nu = 0.3$ . The global critical load  $P_o^C$  can be calculated using Equation (44), whereas the local buckling critical stress  $\sigma_l^C$  can be evaluated using the well-known formula  $\sigma_l^C = k_p D \pi^2 / (b^2 t)$ , where the coefficient  $k_p$  depends on the plate boundary conditions. By increasing the  $c_p$  value, the relative rigidity between the main plate and the stiffener varies from being completely pinned ( $c_p = 0$ ) to fully-fixed ( $c_p \rightarrow \infty$ ). Therefore the limiting values for  $k_p$  are 0.426 or 1.247 for a long stiffener connected to the main plate with one edge free and the edge defining the junction between the stiffener and the main plate being taken to be pinned or fixed respectively (Bulson, 1970). However, the value of the global critical buckling load  $P_o^C$  remains the same since it is independent of  $c_p$ .

To find the equilibrium path in the fundamental and post-buckling states, a similar solution strategy is performed as in recent work (Wadee & Bai, 2014; Wadee & Farsi, 2014), which is illustrated diagrammatically in Figure 5. For a perfect strut, the initial post-

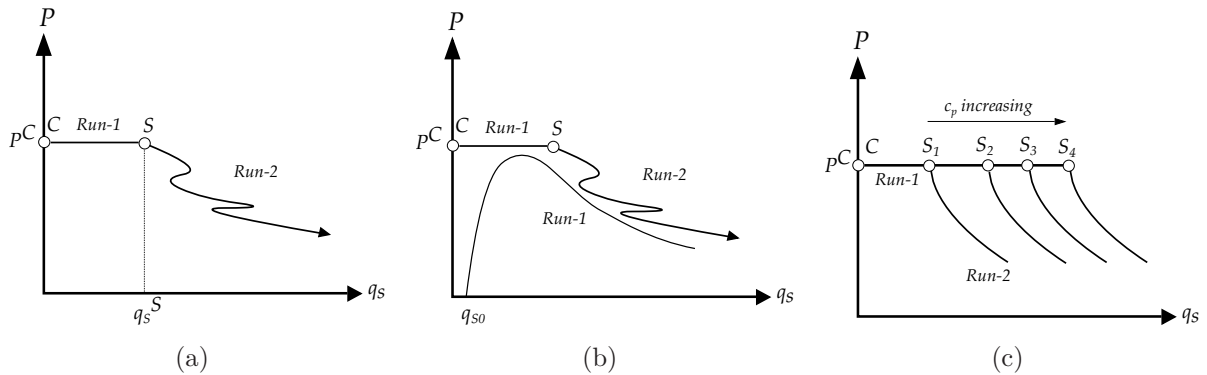


Figure 5: Diagrammatic representation of the sequence of computing the equilibrium paths for the (a) perfect and (b) imperfect cases; (c) shows the perfect cases for different values of  $c_p$  with the corresponding secondary bifurcation points changing as  $c_p$  is increased.

buckling path is computed first from the critical buckling load  $P^C (\equiv P_o^C)$  with  $q_s$  being varied. Many bifurcation points are detected on the weakly stable post-buckling path; the focus being on the one with the lowest value of  $q_s$ , termed the secondary bifurcation point S, see Figure 5(a). Note that the corresponding  $q_s$  value is labelled as  $q_s^S$ . For an imperfect strut, however, the equilibrium path is computed initially from zero axial load and then  $P$  is increased up to the maximum value where a limit point is detected. The load subsequently drops and the path is asymptotic to the perfect path, as shown in Figure 5(b). If the joint stiffness  $c_p$  is varied, the value of  $q_s^S$  would be expected to increase, see Figure 5. This is owing to the local buckling critical stress increasing, which in turn causes the required global mode amplitude to trigger local buckling to increase also.

It is worth noting that for the perfect case, the model is in fact only valid where global buckling or stiffener local buckling is critical since the assumption is made such that the main plate can only buckle in sympathy with the stiffener. For the stiffener local buckling being critical, the bifurcation would occur when  $P = P_l^C$  and a stable post-buckling path would initially emerge from the fundamental path. To include the main plate buckling locally first, the explicit link between  $w_p$  and  $w$  would have to be broken.

Figure 6 shows the numerical results from the example properties stated at the beginning of the current section. Initially, the results are presented for the perfect case where the joint between the main plate and the stiffener is pinned ( $c_p = 0$ ). The graphs in (a–b) show the equilibrium plots of the normalized axial load  $p = P/P_o^C$  versus the generalized coordinates of the sway component  $q_s$  and the maximum out-of-plane normalized deflection of the buckled stiffener ( $w_{\max}/t_s$ ) respectively. The graph in (c) shows the relative amplitudes of global and local buckling modes in the post-buckling range. Finally, the graph in (d) shows the relationship between sway  $q_s$  and tilt  $q_t$  components of the global buckling mode, which are almost equal (difference approximately 0.05%); this indicates that the shear strain is small but, importantly, not zero. As found in Wadee and Farsi (2014), for the case where only the stiffener buckles locally, there is a sequence of snap-backs observed. This is the signature of cellular buckling (Hunt *et al.*, 2000) and the cells are labelled  $C_i$ . Figure 7 shows the corresponding progression of the numerical solutions for the local buckling functions  $w$  and  $u$  for cells  $C_2$ ,  $C_4$ ,  $C_6$  and  $C_8$  defined in Figure 6. It can be seen that the initially localized buckling mode progressively becomes more periodic as the system post-buckling advances.

By comparing the equilibrium paths against those for  $c_p = 0$ , it is observed that the snap-backs begin to vanish as  $c_p$  is increased. Figure 8 shows the equilibrium paths for the strut with an increasingly rigid connection between the plate and the stiffener. In the graphs of the analytical results, the values of  $c_p$ , in Nmm/mm, are taken as 1, 100 and 500 respectively. The graphs in Figure 8(a–b) show the equilibrium path of the normalized axial load  $p = P/P_o^C$  versus the normalized total end-shortening  $\mathcal{E}/L$ , see Equation (29), and the global mode amplitude  $q_s$  respectively. It is found that  $q_s^S$  increases with  $c_p$ ; comparing  $q_s^S$  for the highest  $c_p$  value to the lowest value shown, it is seen to be nearly 50% greater. Moreover, the post-buckling paths show a significantly stiffer response for higher values of  $c_p$ . At  $p = 0.81$ , the maximum out-of-plane displacement  $w$  for  $c_p = 0$  is approximately  $1.65t_s$ , whereas for  $c_p = 500$  Nmm/mm, it is approximately  $1.18t_s$ . Figure 8(c) shows the

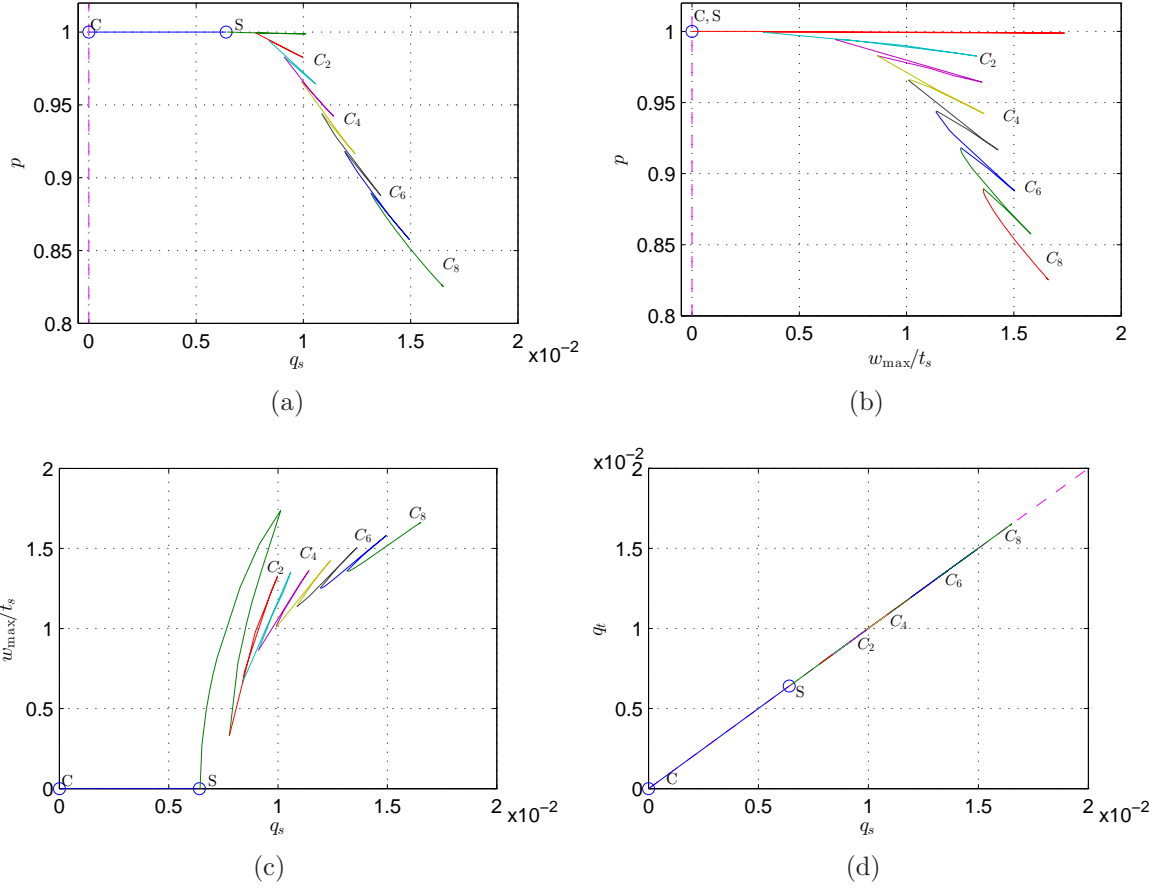


Figure 6: Results for the panel with example properties and assuming the main plate–stiffener joint is pinned ( $c_p = 0$ ). The normalized force ratio  $p = P/P_o^C$  is plotted versus (a) the global mode amplitude  $q_s$  and (b) the normalized maximum out-of-plane deflection of the stiffener  $w_{\max}/t_s$ ; (c) shows the local mode amplitude  $w_{\max}/t_s$  versus the global mode amplitude  $q_s$  in the post-buckling range; (d) shows the relationship between the generalized coordinates  $q_t$  and  $q_s$  that define the global mode.

normalized local versus global mode amplitudes and (d) shows the relationship of the ratio  $\lambda_p$  versus the rotational stiffness  $c_p$ ; the final graph shows that the relationship flattens for larger values of  $c_p$ , which would be expected as a fully rigid joint condition is approached.

## 4 Validation

The commercial FE software package ABAQUS (2011) was first employed to validate the results from the analytical model. The same example set of section and material properties were chosen, as presented in §3. Four-noded shell elements with reduced integration (S4R) were used to model the structure. Rotational springs were also used along the length to simulate the rigidity of the main plate–stiffener joint. An eigenvalue analysis was used to

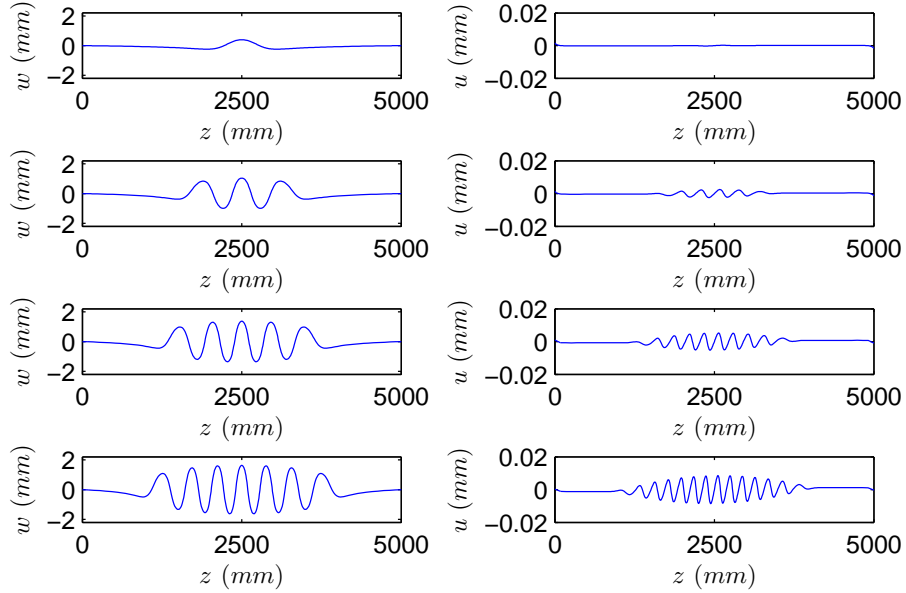


Figure 7: Numerical solutions for the local out-of-plane deflection  $w$  (left) and the local in-plane deflection  $u$  (right) showing the progressive spreading of the stiffener local buckling profile for cells  $C_2$ ,  $C_4$ ,  $C_6$  and  $C_8$  (top to bottom respectively) from the perfect model.

calculate the critical buckling loads and eigenmodes. The nonlinear post-buckling analysis was performed with the static Riks method (Riks, 1972) with the aforementioned eigenmodes being used to introduce the necessary geometric imperfection to facilitate this. In the current example, the rotational spring stiffness  $c_p$  is assumed to be 1000 Nmm/mm, which gives a value of  $\lambda_p = 0.2687$  and gives negligible rotation at the main plate–stiffener connection. Linear buckling analysis shows that global buckling is the first eigenmode; Table 1 presents the critical stresses for all the components from the analytical and the FE

Source	$\sigma_o^C$ (N/mm <sup>2</sup> )	$\sigma_{l,s}^C$ (N/mm <sup>2</sup> )	$\sigma_{l,p}^C$ (N/mm <sup>2</sup> )	Critical mode
Theory	4.948	236.02	539.91	Global
FE	4.942	228.94	503.15	Global
% difference	0.12	3.09	7.31	N/A

Table 1: Theoretical and FE values of the global and local critical buckling stresses ( $\sigma_o^C$  and  $\sigma_l^C$ ) respectively; subscripts “ $p$ ” and “ $s$ ” refer to the main plate and the stiffener respectively and  $k_p$  is taken to be 1.247 for the stiffener and 6.97 for the main plate (assuming a rigid joint exists at the main plate–stiffener connection). The expression for  $\sigma_o^C = P_o^C/A$ , where  $A$  is the cross-sectional area of the strut.

models.

Figure 9 shows the comparisons between the numerical results from the analytical and the FE models. It is shown for the case with an initial global imperfection  $q_{s0} = 0.001$

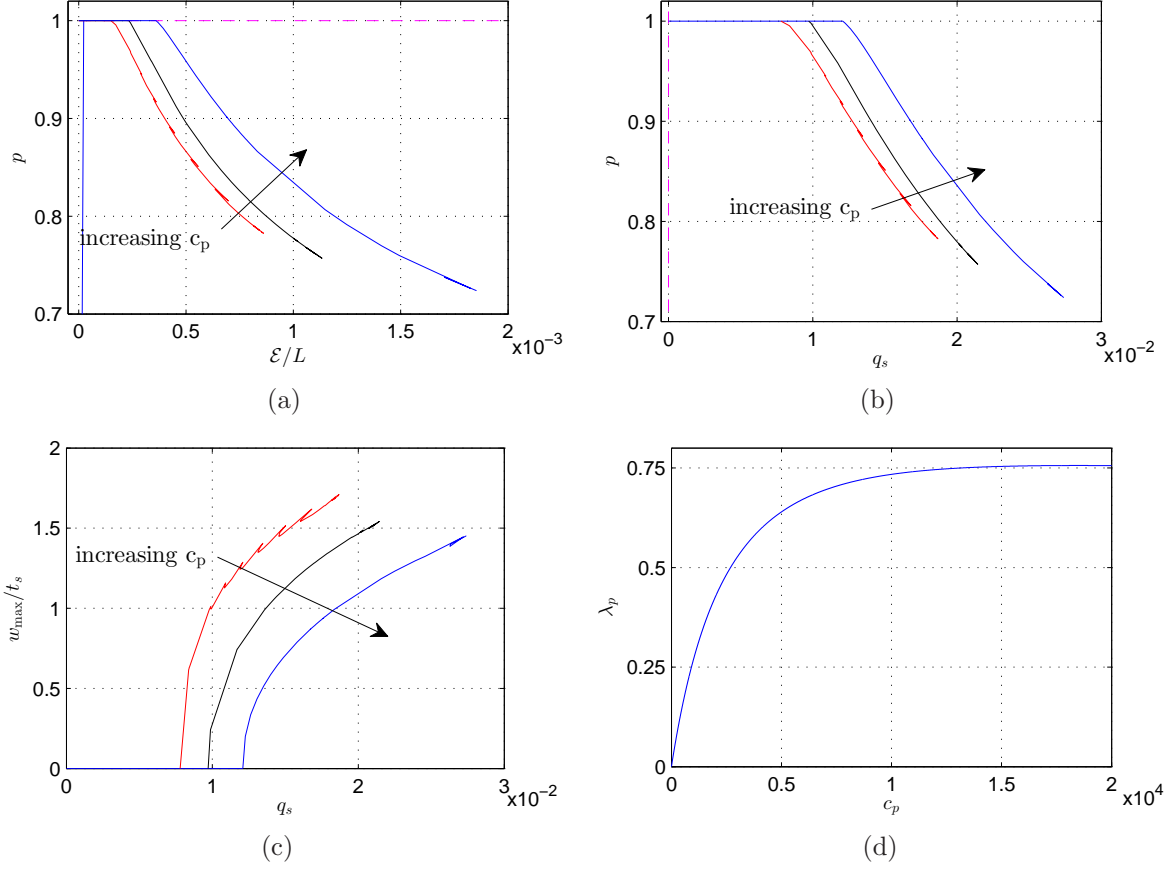


Figure 8: Variation of the equilibrium paths for increasing rigidities of the main plate–stiffener joint ( $c_p = 1, 100, 500$  Nmm/mm). Graphs show the normalized force ratio  $p$  versus (a) the normalized end-shortening, (b) the global mode amplitude  $q_s$ ; (c) shows the local versus global mode amplitudes. (d) Plot of the ratio of the out-of-plane displacements in the main plate to the stiffener  $\lambda_p$  versus  $c_p$  in Nmm/mm.

and a local imperfection, where  $A_0 = 0.12$  mm,  $\alpha = 5.0$ ,  $\beta = 75$  and  $\eta = L/2$  for  $w_0$ , which represents the initial imperfection for the analytical model that matches the FE model imperfection satisfactorily such that a meaningful comparison can be made. The graphs in (a–b) show the normalized axial load  $p$  versus the global and the local mode amplitudes respectively; the graph in (c) shows the local versus the global buckling modal amplitudes. Figure 10 shows the local out-of-plane deflection profiles  $w$  at the respective locations (i)–(iii), shown in Figure 9(a–c), the comparison being for the same value of  $p$ . As can be seen, both sets of graphs show excellent correlation in all aspects of the mechanical response; in particular, the results for  $w$  from the analytical and the FE model are almost indistinguishable. This shows a marked improvement on the previous simpler model (Wadee & Farsi, 2014) where the main plate was assumed not to buckle locally. A visual comparison between the 3-dimensional representations of the strut from the analytical and the FE models is also presented in Figure 11.

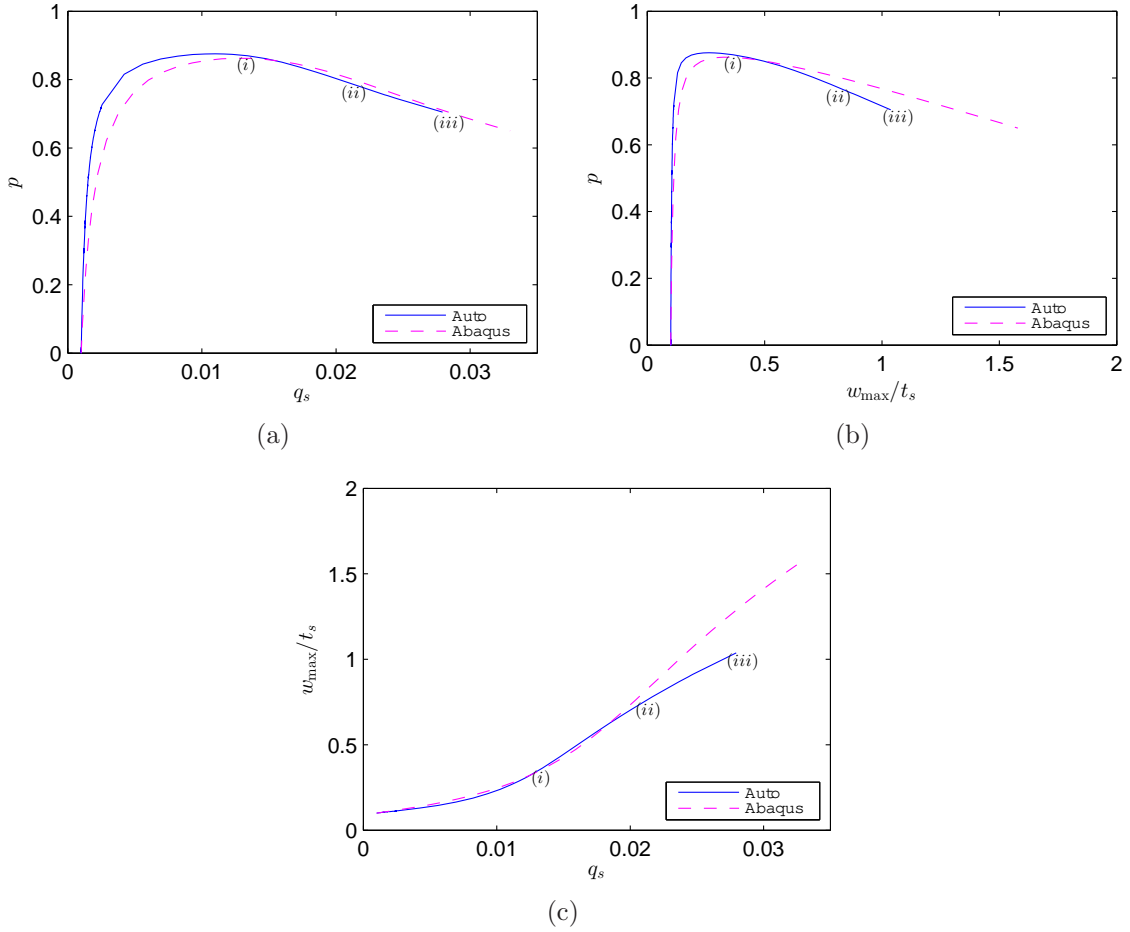


Figure 9: Comparisons of the analytical model (solid lines) versus the FE model (dashed lines) solutions, both with  $c_p = 1000$  Nmm/mm. The plots show the normalized force ratio  $p$  versus (a) the global mode amplitude  $q_s$  and (b) the maximum out-of-plane normalized stiffener deflection  $w_{\max}/t_s$ ; (c) local versus global mode amplitudes.

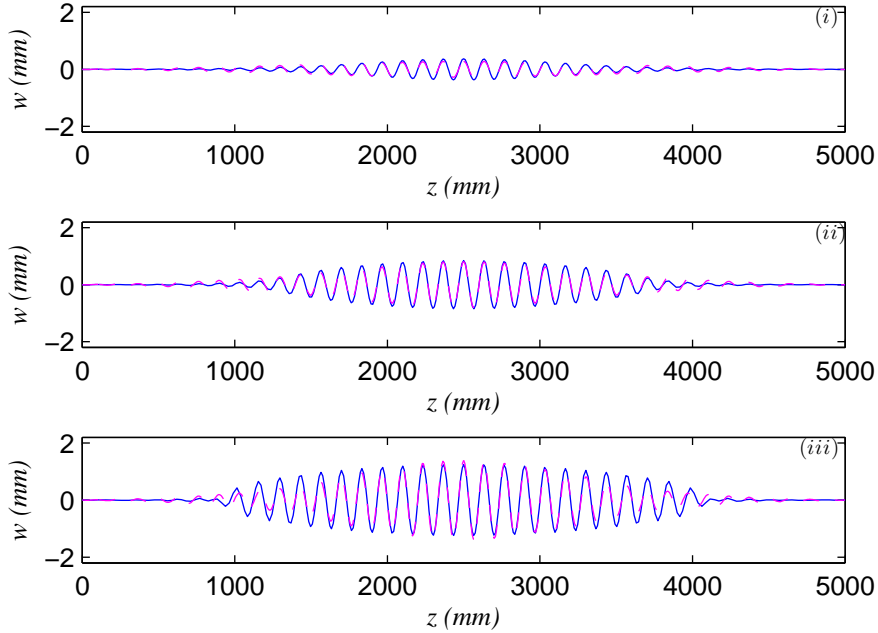


Figure 10: Comparisons of the analytical model (solid lines) versus the FE model (dashed lines) solutions for the out-of-plane deflection of the stiffener  $w$  for the points shown in (i)–(iii).

#### 4.1 Comparison with experimental study

An experimental study of a thin-walled stiffened plate conducted by Fok *et al.* (1976) also focused on the case where global buckling was critical. Two specific tests were conducted on a panel with multiple stiffeners. The experimental results were compared with the current analytical model and also with the FE model formulated in ABAQUS. The cross-section of the stiffened panel investigated is shown in Figure 1. The experimental panel had 10 blade stiffeners with spacing  $b = 45.5$  mm, height  $h_1 = 13.5$  mm, thicknesses  $t_s = t_p = 0.735$  mm and  $h_2 = t_p/2$  (*i.e.* stiffeners on one side only). The experimental specimen was constructed from cold-setting Araldite<sup>®</sup> (epoxy resin) and the material had an elastic stress–strain relationship, but no material properties were provided. Hence, in the analytical and FE models, nominal values of  $E$  and  $\nu$  were used ( $E = 210$  kN/mm<sup>2</sup> and  $\nu = 0.3$  as before); this did not pose a problem so long as the same values were used in both models. Moreover, it is worth noting that the behaviour of the experimental specimens was reported to be elastic and only ratios of loads and displacements were reported as the results (Fok *et al.*, 1976).

In the first test, the length  $L$  of the panel was 400 mm ensuring that the global critical buckling load was much less than the local buckling load. The initial global imperfection was measured to be  $W_0 = 1.2t_s$  but there were negligible out-of-plane imperfections in the stiffeners and in the main plate (*i.e.*  $w_0 = w_{p0} = 0$  were assumed). In the second test, the length of the stiffened panel was reduced to  $L = 320$  mm with the consequence that

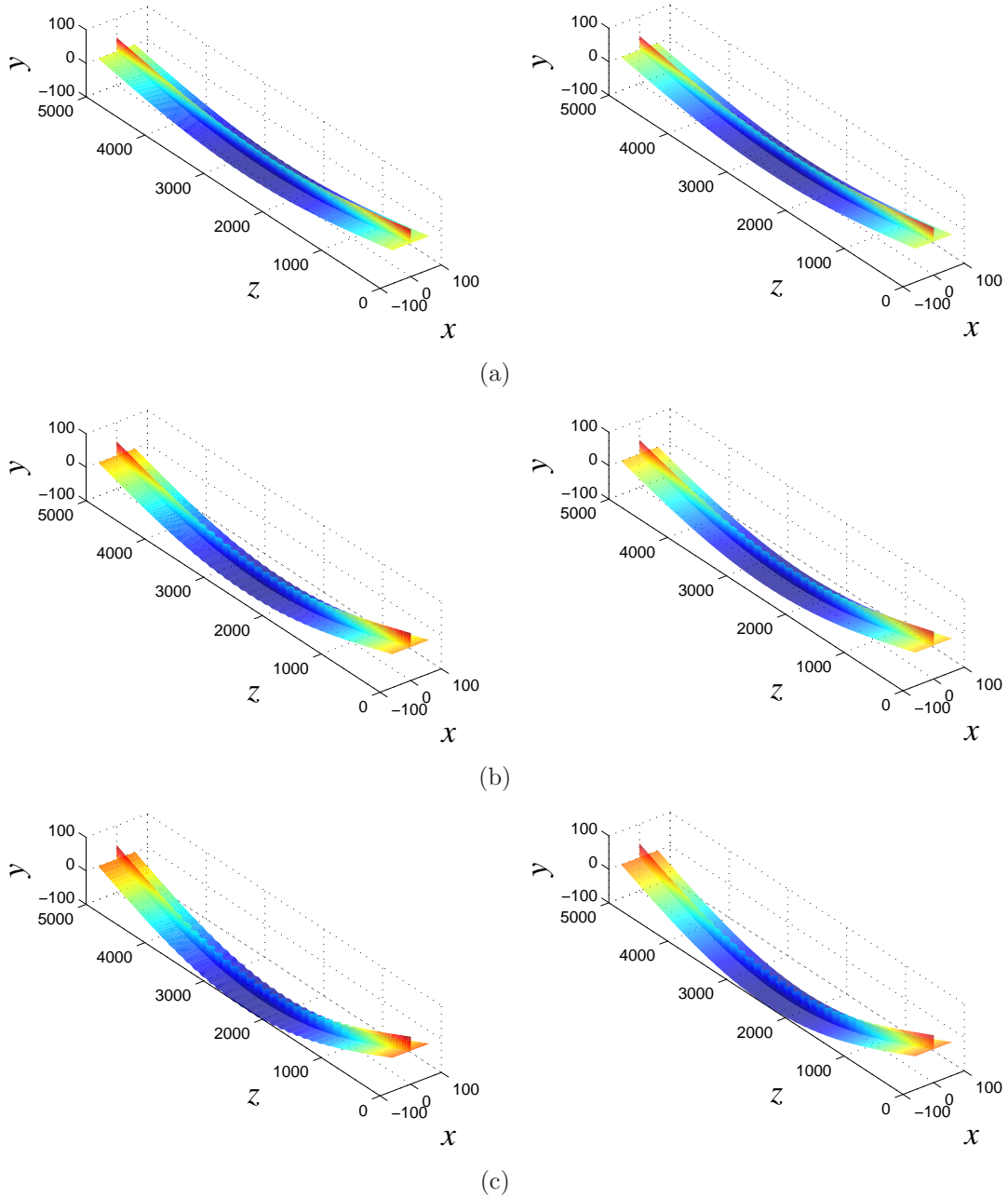


Figure 11: Comparisons of the numerical solutions from (left) the analytical model and (right) the FE model with  $c_p = 1000$  Nmm/mm visualized on 3-dimensional representations of the strut. The results are shown for equilibrium states at the points shown in Figure 9(a–c) defined as (i)–(iii). All dimensions are in millimetres but the local buckling displacements are scaled by a factor of 2 to aid visualization.

the local buckling stress was only approximately 5% above that for the global mode. The corresponding critical stresses for both tests are summarized in Table 2.

	$L$ (mm)	$\sigma_o^C$ (N/mm <sup>2</sup> )	$\sigma_{l,s}^C$ (N/mm <sup>2</sup> )	$\sigma_{l,p}^C$ (N/mm <sup>2</sup> )
Test 1	400	$7.122 \times 10^{-4}E$	$3.34 \times 10^{-3}E$	$1.176 \times 10^{-3}E$
Test 2	320	$1.109 \times 10^{-3}E$	$3.34 \times 10^{-3}E$	$1.176 \times 10^{-3}E$

Table 2: Theoretical values of the global and local critical buckling stresses ( $\sigma_o^C$  and  $\sigma_l^C$ ) respectively; subscripts “ $p$ ” and “ $s$ ” refer to the main plate and the stiffener respectively. The expression for  $\sigma_o^C = P_o^C/A$ , where  $A$  is the cross-sectional area of the panel.

For the  $L = 320$  mm panel, the initial global buckling mode imperfection  $W_0$  was set to  $0.8t_s$  and the amplitude of the out-of-plane imperfection  $A_0 = 0.01t_s$  with  $\alpha = 4$ ,  $\beta = 11$  and  $\eta = L/2$ . For both models, analytical and FE, the stiffness of the rotational spring  $c_p$  was calibrated to be 300 Nmm/mm since this gave the best match with the peak load of the experimental results. To find the equilibrium path, the numerical continuation process was initiated from zero load. Figure 12 shows the comparisons between the experimental

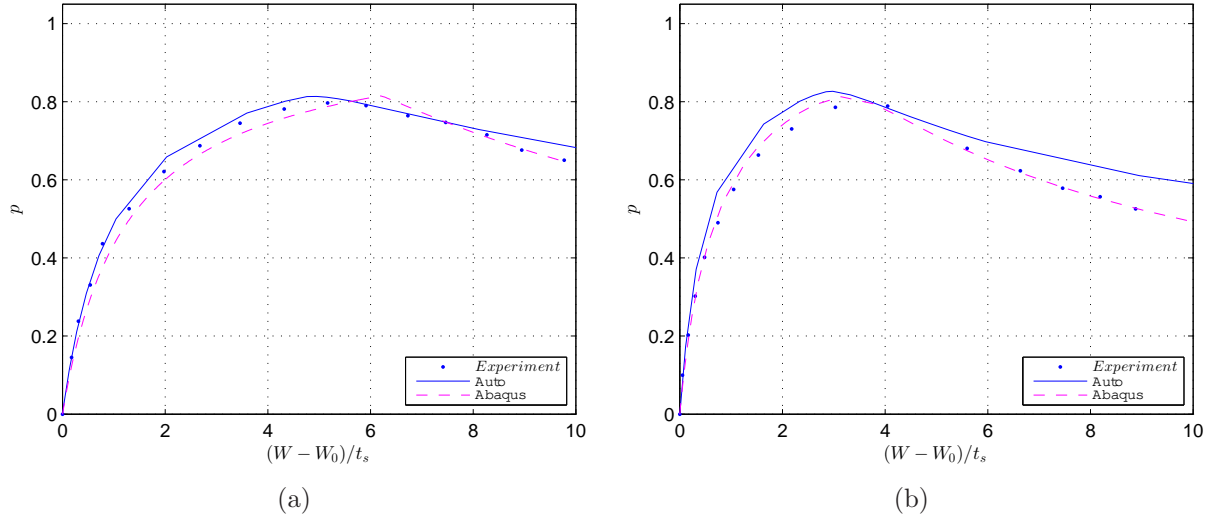


Figure 12: Comparisons of the experimental results (dots) with the solutions from the analytical model (solid lines) and the FE model (dashed lines). Graphs of the normalized force ratio  $p$  versus the normalized global mode deflection relative to the initially imperfect state for the panel  $(W - W_0)/t_s$  are shown for (a) Test 1 where  $L = 400$  mm and (b) Test 2 where  $L = 320$  mm.

results from Fok *et al.* (1976), the analytical and the FE models. The comparisons show strong agreement between all three sets of results. Since there was no information provided about the local out-of-plane deflection magnitude, the results from the analytical model are compared to the FE results directly. Figure 13(a) presents the comparison of the normalized force ratio  $p = P/P_o^C$  versus the maximum normalized out-of-plane stiffener

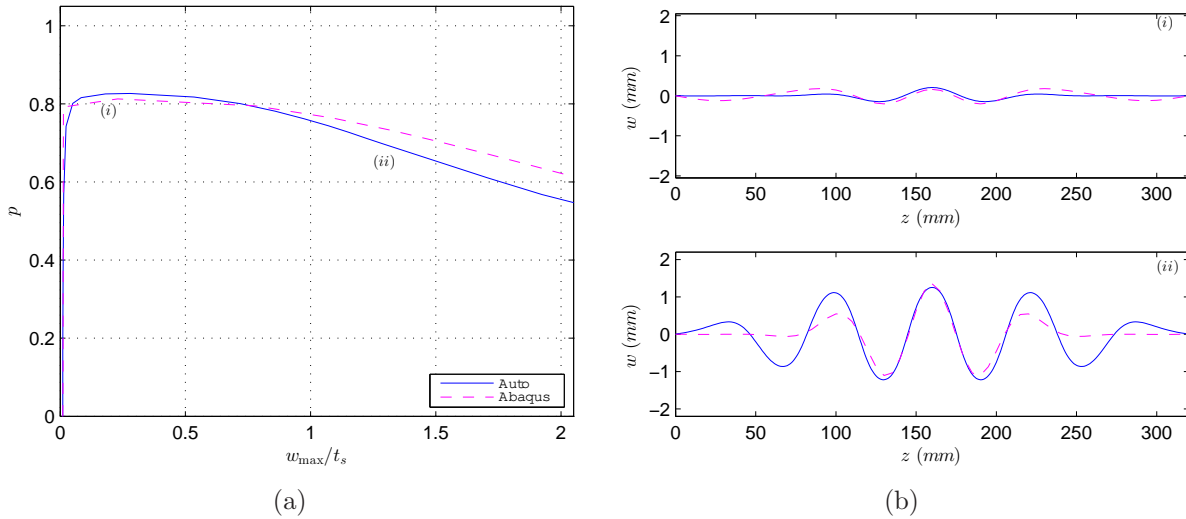


Figure 13: Comparison of the analytical results (solid lines) with the FE model (dashed lines) for the Test 2 properties. (a) Plot of the normalized force ratio  $p = P/P_o^C$  versus the normalized maximum out-of-plane deflection  $w_{\max}/t_s$ . (b) Local buckling out-of-plane deflections  $w$  of the stiffener for the points shown in (i) and (ii).

deflection  $w_{\max}/t_s$ , where the initial global and local imperfection sizes and shapes were given as before. Figure 13(b) shows the comparisons of the analytical with the FE model results for the local out-of-plane displacement of the stiffener  $w$  for the Test 2 properties. Note that the results are obtained when (i)  $p = 0.80$  and (ii)  $p = 0.65$ . The comparison between the local buckling amplitudes and wavelength is excellent. Of course at lower loads, in the advanced post-buckling range, there is divergence between the non-midspan peaks; this is a further example of the FE model locking the modal wavelength as found in earlier studies even though actual experimental evidence shows the contrary (Becque, 2008; Wadee & Gardner, 2012; Wadee & Bai, 2014; Wadee & Farsi, 2014).

## 5 Concluding remarks

An analytical model based on variational principles has been extended to model local-global mode interaction in a stiffened plate subjected to uniaxial compression. By introducing the sympathetic deflection of the main plate along with the locally buckling stiffener, the current model could now be compared to published experiments (Fok *et al.*, 1976) and a finite element model formulated in ABAQUS; results from both are found to be excellent. Currently, the authors are conducting an imperfection sensitivity study to quantify the parametric space for designers to avoid such dangerous structural behaviour, the results of which would provide greater understanding of the interactive buckling phenomena and highlight the practical implications.

## References

- ABAQUS. 2011. *Version 6.10*. Providence, USA: Dassault Systèmes.
- Bai, L., & Wadee, M. A. 2014. Mode interaction in thin-walled I-section struts with semi-rigid flange-web joints. *Int. J. Non-Linear Mech.* Submitted.
- Becque, J. 2008. *The interaction of local and overall buckling of cold-formed stainless steel columns*. Ph.D. thesis, School of Civil Engineering, University of Sydney, Sydney, Australia.
- Becque, J., & Rasmussen, K. J. R. 2009. Experimental investigation of the interaction of local and overall buckling of stainless steel I-columns. *Asce journal of structural engineering*, **135**(11), 1340–1348.
- Budiansky, B. (ed). 1976. *Buckling of structures*. Berlin: Springer. IUTAM symposium.
- Bulson, P. S. 1970. *The stability of flat plates*. London, UK: Chatto & Windus.
- Burke, J., & Knobloch, E. 2007. Homoclinic snaking: Structure and stability. *Chaos*, **17**(3), 037102.
- Butler, R., Lillico, M., Hunt, G. W., & McDonald, N. J. 2000. Experiment on interactive buckling in optimized stiffened panels. *Structural and Multidisciplinary Optimization*, **23**(1), 40–48.
- Chapman, S. J., & Kozyreff, G. 2009. Exponential asymptotics of localised patterns and snaking bifurcation diagrams. *Physica D*, **238**(3), 319–354.
- Doedel, E. J., & Oldeman, B. E. 2011. *Auto-07p: Continuation and bifurcation software for ordinary differential equations*. Montreal, Canada: Concordia University.
- Fok, W. C., Rhodes, J., & Walker, A. C. 1976. Local buckling of outstands in stiffened plates. *Aeronautical Quarterly*, **27**, 277–291.
- Ghavami, K. G., & Khedmati, M. R. 2006. Numerical and experimental investigation on the compression behaviour of stiffened plates. *J. Constr. Steel Res.*, **62**(11), 1087–1100.
- Grondin, G. Y., Elwi, A. E., & Cheng, J. 1999. Buckling of stiffened steel plates – a parametric study. *J. Constr. Steel Res.*, **50**(2), 151–175.
- Guarracino, F., & Walker, A. 1999. *Energy methods in structural mechanics*. Thomas Telford.
- Hancock, G. J. 1981. Interaction buckling in I-section columns. *ASCE J. Struct. Eng.*, **107**(1), 165–179.

- Hunt, G. W., & Wadee, M. A. 1998. Localization and mode interaction in sandwich structures. *Proc. R. Soc. A*, **454**(1972), 1197–1216.
- Hunt, G. W., Da Silva, L. S., & Manzacchi, G. M. E. 1988. Interactive buckling in sandwich structures. *Proc. R. Soc. A*, **417**(1852), 155–177.
- Hunt, G. W., Peletier, M. A., Champneys, A. R., Woods, P. D., Wadee, M. A., Budd, C. J., & Lord, G. J. 2000. Cellular buckling in long structures. *Nonlinear Dyn.*, **21**(1), 3–29.
- Koiter, W. T., & Pignataro, M. 1976. *A general theory for the interaction between local and overall buckling of stiffened panels*. Tech. rept. WTHD 83. Delft University of Technology, Delft, The Netherlands.
- Loughlan, J. (ed). 2004. *Thin-walled structures: Advances in research, design and manufacturing technology*. Taylor & Francis.
- Murray, N. W. 1973. Buckling of stiffened panels loaded axially and in bending. *The Structural Engineer*, **51**(8), 285–300.
- Pignataro, M., Pasca, M., & Franchin, P. 2000. Post-buckling analysis of corrugated panels in the presence of multiple interacting modes. *Thin-Walled Struct.*, **36**(1), 47–66.
- Riks, E. 1972. Application of Newton’s method to problem of elastic stability. *Trans. ASME J. Appl. Mech.*, **39**(4), 1060–1065.
- Ronalds, B. F. 1989. Torsional buckling and tripping strength of slender flat-bar stiffeners in steel plating. *Proc. Instn. Civ. Engrs.*, **87**(Dec.), 583–604.
- Schafer, B. W. 2002. Local, distortional, and Euler buckling of thin-walled columns. *ASCE Journal of Structural Engineering*, **128**(3), 289–299.
- Sheikh, I. A., Grondin, G.Y., & Elwi, A. E. 2002. Stiffened steel plates under uniaxial compression. *J. Constr. Steel Res.*, **58**(5–8), 1061–1080.
- Thompson, J. M. T., & Hunt, G. W. 1973. *A general theory of elastic stability*. London: Wiley.
- Thompson, J. M. T., & Hunt, G. W. 1984. *Elastic instability phenomena*. London: Wiley.
- Wadee, M. A. 2000. Effects of periodic and localized imperfections on struts on nonlinear foundations and compression sandwich panels. *Int. J. Solids Struct.*, **37**(8), 1191–1209.
- Wadee, M. A., & Bai, L. 2014. Cellular buckling in I-section struts. *Thin-Walled Struct.*, **81**, 89–100.
- Wadee, M. A., & Farsi, M. 2014. Cellular buckling in stiffened plates. *Proc. R. Soc. A*, **470**(2168), 20140094.

- Wadee, M. A., & Gardner, L. 2012. Cellular buckling from mode interaction in I-beams under uniform bending. *Proc. R. Soc. A*, **468**(2137), 245–268.
- Wadee, M. A., & Hunt, G. W. 1998. Interactively induced localized buckling in sandwich structures with core orthotropy. *Trans. ASME J. Appl. Mech.*, **65**(2), 523–528.
- Wadee, M. A., Yiatros, S., & Theofanous, M. 2010. Comparative studies of localized buckling in sandwich struts with different core bending models. *Int. J. Non-Linear Mech.*, **45**(2), 111–120.
- Wadee, M. K., Hunt, G. W., & Whiting, A. I. M. 1997. Asymptotic and Rayleigh–Ritz routes to localized buckling solutions in an elastic instability problem. *Proc. R. Soc. A*, **453**(1965), 2085–2107.
- Woods, P. D., & Champneys, A. R. 1999. Heteroclinic tangles and homoclinic snaking in the unfolding of a degenerate reversible Hamiltonian–Hopf bifurcation. *Physica D*, **129**(3–4), 147–170.